Peer-reviewed version available at *Coatings* **2018**, *8*, 247; doi:10.3390/coatings8070247

Article

Structure and properties of high-hardness silicide coatings on cemented carbides for high temperature applications

Samuel Humphry-Baker[1] and Jessica Marshall[2,3]

[1] Department of Materials, Imperial College London, Prince Consort Road, London SW7 2BP, UK; s.humphry-baker@imperial.ac.uk

[2] Sandvik Hyperion, Pol. Ind. Roca, C/ Verneda s/n, 08107 Martorelles, Barcelona, Spain.

[3] Materials and Analytical Sciences, Department of Physics, University of Warwick, Coventry, CV4 7AL, UK j.marshall.4@warwick.ac.uk

*Correspondence: j.marshall.4@warwick.ac.uk; Tel: +44 (0) 2476 151783

An oxidation resistant coating on cemented tungsten carbides is characterised in this work. Cemented tungsten carbides (cWCs) are routinely used in mining and manufacturing but are also candidate materials for compact radiation shielding in fusion power generation. In both environments, cWCs will suffer significant degradation due to oxidation at relatively low temperatures. In a recent study, a Si-deposition coating method was demonstrated to improve the oxidation resistance of cWCs by up to a factor of 1,000. This work focusses on the growth kinetics, phase composition, and mechanical properties of these coatings. By combining quantitative X-ray diffraction, electron microscopy and nanoindentation, we show that the coating layer has a 20 % higher hardness than the substrate, which was explained on the basis of a previously-unknown presence of a fine distribution of very hard SiC laths. To interpret the coating stability, a coating growth map is developed. The map shows the structure is stable under a broad range of processing temperatures and composite compositions, demonstrating the potential application of these coatings in a variety of nuclear shielding cWCs.

Keywords: Cemented carbides, cermets, iron binders, oxide coating, radiation shielding, nanoindentation, passivation, silicides.

1. Introduction

Nuclear fusion power is rapidly developing through recent advances in high temperature superconductors and the development of compact spherical fusion tokamaks [1]. Because of the smaller scales of these devices, there is an increasing emphasis on enhancing the efficiency of shielding materials, which must resist a wide variety of ionizing radiation and extreme conditions that may be experienced over a typical duty cycle. One such condition, which is the focus of this paper, is a loss-of-coolant event whereby materials may be exposed to oxygen at high temperatures. The oxide layer formed in this scenario must be stable so as not to release any potentially hazardous materials into the environment. Such a scenario may also be relevant when considering shielding materials in conventional nuclear reactors.

A potential candidate material for next generation nuclear shielding is cemented tungsten carbide (cWC). cWCs have excellent wear and thermal properties along with high hardness and impressive fracture toughness [2]. The properties of cWCs result from their combination of fine WC particles (0.4-8μm) and ductile metallic binder phase processed using powder metallurgy. It also has promising shielding characteristics compared to tungsten metal, which will be used extensively as a shielding material for ITER [3]. The good performance of WC is due to the high neutron and gamma ray reflectance of W and the neutron moderation role of C. Furthermore, it is not an activation hazard. Hence WC is a promising material for radiation shielding and has been recently shown computationally to have excellent neutronics properties [4] [5].

Historically, pure WC had been used for laboratory scale nuclear shielding during the Manhatten Project [6] but its deployment in fusion reactor shielding has been limited. Some of the practical limitations on its use are as follows. Firstly, the manufacture of pure WC compacts is a challenge, often leading to porous (~90% dense) materials. When such porous WC is compared with fully dense W metal, it has showed significantly less resistance to oxidation than W metal [6]. However, recent data on fully dense WC samples [7] shows a marked improvement in oxidation resistnace. Another problem is that the most common binder metals used for cWCs, Co and Ni, are both activation hazards under fusion-relevant irradiation conditions. Thus, research in cWCs for fusion applications has not been extensive. Recently however, a Fe-Cr alloy consisting of 92wt% Fe and 8 wt% Cr (Fe-8Cr) [8] has been identified as a promising cWC binder phase. Fe-8Cr does not activate significantly, unlike Co and Ni, and can be manufactured without the flammability risk during processing that pure Fe metal powder would have during powder processing and spray drying.

A remaining challenge facing the use cWC as nuclear shielding is its accident tolerance. cWCs suffer significant degradation in their properties at prolonged high temperatures in the presence of oxygen. Growth of an oxide layer becomes significant at prolonged exposure to T > 600°C along with decreases in hardness and bulk modulus [2]. Their oxidation tendency could be problematic because the oxides of WC are volatile at high temperatures. Thus in a worst-case scenario where coolant fails and parts of the hot shielding are exposed to air, the plasma-facing components of the shielding could reach temperatures of 1000°C or greater [9]. Materials must withstand this scenario without the formation of volatile oxides and dissemination of hazardous radiation products. In a recent work, we demonstrated a coating method for cWCs based on silicon impregnation, which can enhance its oxidation resistance and prevent formation of volatile species [10]. The coating improved the oxidation resistance by 3 orders of magnitude and was stable up to 1200°C. The mechanism behind the protective effect of the Si-based coating was the formation of a Fe-rich silicide outer layer, which readily formed a SiO_2 passivation layer, unlike WSi_2, which is known to oxidise in an active manner over the same temperature range.

In this paper we have characterised the mechanical properties of the coating for the first time. Our measurements reveal a surprising result: the coating formed a superhard protective layer of about 20 % harder than the substrate. This is unexpected since the main constituent, i.e. WSi_2, is softer than the WC phase. However, this result can be explained based on the formation of very hard SiC laths, which were not discovered in our previous work [11]. Beneath the coating, a porous region results in a 3 GPa hardness drop, which is due to preferential migration of the FeCr binder to the surface. Potential treatments to mitigate the effect of this layer are discussed.

2. Materials and Methods

2.1 Materials Preparation

The cWC sample used for Si impregnation was a medium-fine WC ($d_{50, WC}$ = 0.8 μm) with a 10 wt% Fe-8Cr binder. All hardmetals were produced using a laboratory scale powder metallurgy process [9,10] simulating the larger scale industrial process route. The WC (Wolfram Bergbau) and Fe-8Cr (pre-alloyed spray atomized powder d_{50} = 7 μm by Osprey) powder charge was set to 100g (90 g WC: 10g Fe-8Cr). No carbon additions were used, although the effect of carbon content was evaluated by calculating the phase diagrams for the W-C-FeCr system using Thermocalc (©Thermocalc AB) with carbon content as the dependant variable. Powders were placed in a 0.25l WC-lined mill and ball milled with WC media with a media : charge mass ratio of 12:1 in 50 ml ethanol with an organic binder. Powders were dried and pressed at a pressure of 19 MPa to for a plate with sintered dimensions 40 mm x 25 mm x 5 mm. The Si coating on selected WC-Fe-8Cr samples (hereafter referred to as the substrate) was performed by the pack cementation method [11]. The pellet and powder pack (Si and NaF) were loaded into a lidded alumina crucible and heated to 1000°C in flowing Ar-5% H_2 for a 4 h dwell. Further details of this process can be found in a previous study [8].

2.2 Characterization

Post sintering, sample were tested to evaluate sintered density, hardness and toughness. Sample microstructure was evaluated using optical and scanning electron microscopy (SEM) using a Zeiss SUPRA55-VP microscope. High-resolution images of the coating were acquired on a ZEISS LEO Gemini 1525 field emission gun SEM. Energy dispersive x-ray analysis (EDX) was performed using an Oxford Instruments DryCool detector with a 15mm working distance and an accelerating voltage of 30kV using Oxford Instruments INCA software. Microstructural parameters such as the median grain size (WC d_{50}) and phase identification were evaluated by electron backscatter diffraction (EBSD) using a Nordlys detector with an accelerating voltage of 21kV and a 60μm beam aperture. Data was acquired with the Oxford Instruments AZtec software and Channel 5 Tango post-processing module. Further details on preparation and analytical methods used for WC grain size measurements are described in detail in previous work. X-ray diffraction (XRD) was performed on a Panalytical X'Pert powder diffractometer with Cu radiation source operated at 40 kV and 40 mA. Patterns were analysed using the Rietveld method, employing a pseudo-Voight profile function. XRD patterns taken through the depth of the coating were achieved by sectioning the surface via manually polishing 5μm intervals from the coating surface, using 1200 grit SiC paper. Coating removal was measured using a digital micrometer. Instrumented hardness measurements were carried out on a Micromaterials Nanotest platform at room temperature, using a Vickers diamond indenter, whose area function was calibrated on an amorphous silicon substrate. The indenter load was applied over a 10s load; a 30s dwell period, and a 10s unload. Thermal drift was corrected for by a 30 s drift correction post indentation. The hardness was calculated using the Oliver-Pharr method [12]. Indents were imaged using a JSM 6010 SEM operated in secondary electron imaging (SEI) mode.

Preprints (www.preprints.org) | NOT PEER-REVIEWED | Posted: 1 May 2018 doi:10.20944/preprints201805.0005.v1

Peer-reviewed version available at Coatings 2018, 8, 247; doi:10.3390/coatings8070247

3. Results and discussion

3.1 As-sintered WC-Fe-8Cr materials

We first assess the substrate as its properties will later be compared to the coatings. Properties of the substrate including hardness, toughness and median grain size d_{50} are given in Table 1:

Sample	Shrinkage	Density	Sintered WC d_{50}	HV30	$K1_c$
	%	g cm^{-3}	µm	kgf mm^{-2}	MPa m$^{0.5}$
10wt% Fe-8Cr	17.7	14.14	0.8	1490	8.2

Table 1: Physical properties of as-sintered cWC material

The as-sintered material shows shrinkage and toughness values in line with conventional cWCs of the same grain size and binder content. WC-Fe substrates were fully dense with an upper limit to porosity being 0.2 vol% as measured by optical microscopy using ISO 4499-3:2016 porosity assessment standards. Hardness is slightly higher and toughness lower in WC-Fe-8Cr than for a WC-Co material with equivalent grain size and binder content. The reasons for this are twofold: (1) Fe and Cr tend to limit Ostwald ripening during liquid phase sintering relative to Co [8], leading to a finer sintered grain size for the same WC powder and (2) Brittle ternary phases such as M_6C (M = W, Fe(Cr)) form more readily in Fe-based binder systems [8, 11] relative to Co or Ni-based binders. The formation of ternary phases in WC-Fe-8Cr can be controlled via carbon content as is currently used for conventional WC-Co materials [2, 13-15]. In this work, no carbon compensation was used for WC-Fe-8Cr to establish a baseline material for further work on this system. The effect of this lack of carbon correction is shown in Figure 1.

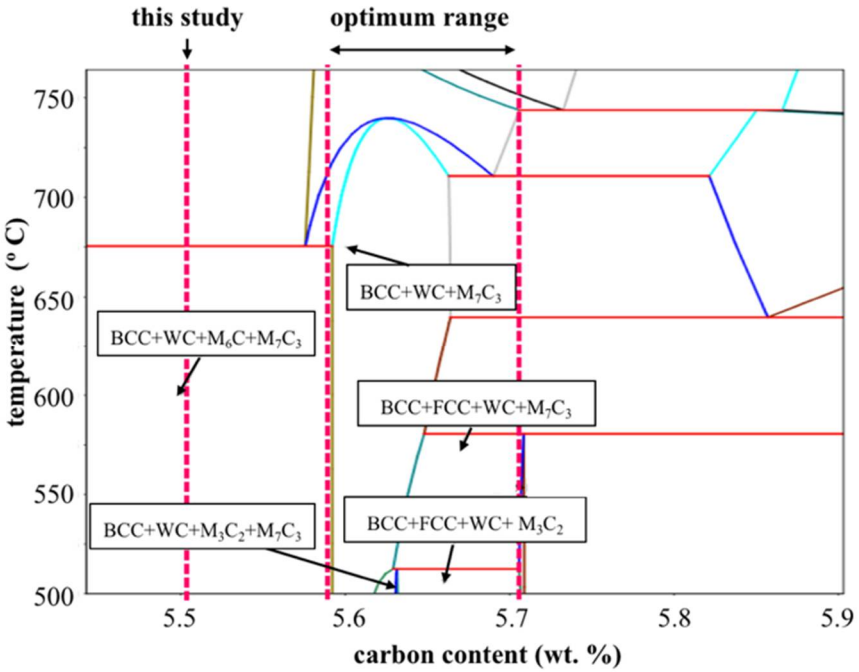

Figure 1: Phase diagram of the WC-Fe-8Cr system as a function of temperature and carbon weight fraction. Although no two-phase region exists, there is a desired region of BCC+WC+M_7C_3. The dotted lines indicate this optimal region of carbon content (about 5.6-5.7 wt. %) vs. the carbon content for substrate materials in this study (5.5 wt. %).

Figure 1 shows part of the WC-Fe-8Cr phase diagram, as calculated using Thermocalc, with respect to carbon content and temperature. Unlike Co or Ni-based cWCs – which both contain a broad binder+WC region – there is no true two-phase (binder+WC) region in WC-Fe-8Cr. This is because Fe has a stronger affinity for carbon than Ni or Co. Instead of a two-phase region there is a "BCC+WC+M_7C_3" region, at about 5.6-5.7 wt.% C, whereby the formation of mixed metal carbides is present but mitigated. The material used in this study was not within this preferred region, since the carbon content was around 5.5 wt. %. Thus, the formation of other mixed-metal carbide phases such as M_6C is predicted which tend to reduce both hardness and toughness overall.

Figure 2 shows (a) secondary electron and (b) EBSD images of the microstructure of the WC-Fe-8Cr substrate. For phase identification, indexed data was processed by single pixel removal and a single iteration grain dilation (> 4 nearest neighbours). WC grain boundaries were defined as regions where the average orientation difference was > 8°. Figure 2 also shows how the grain size was established using EBSD. Median WC grain size d_{50} was calculated from the linear diameter obtained from EBSD orientation image mapping of the WC phase, details of which are given in [15].

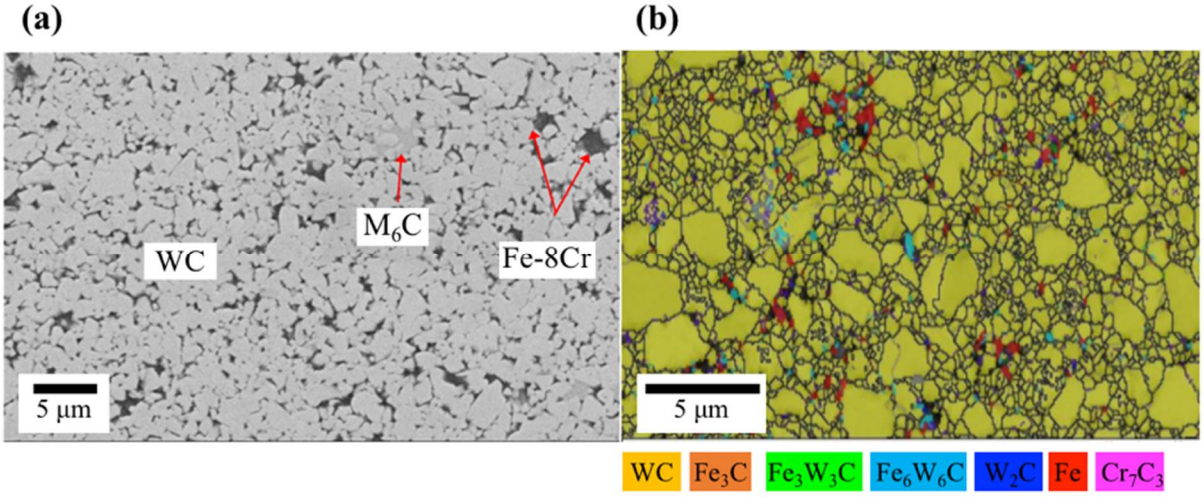

Figure 2: SEI image (**a**) in secondary electron of untreated WC-Fe-8Cr cWC. M_6C is present as intermediate contrast between high-Z WC (light grey) and low-Z Fe-8Cr (dark grey). Image (**b**) shows an EBSD phase map showing the WC (yellow) and BCC binder pools (red) along with M_6C (Fe_3W_3C). Unindexed points are shown in grey.

The microstructure of the baseline Fe-8Cr cWC is similar to that of other cWCs with transition metal binders although grain size is rather non-uniform. This is due to Fe and Cr inhibiting Ostwald ripening, resulting in a considerable volume fraction of fine grains. Therefore, WC d_{50} (0.8 µm) is significantly lower than the target d_{50} of the starting WC powder (2 µm). M_6C formation consumes the WC phase, leading to more binder lakes and a more irregular structure than in a carbon-optimized material. M_6C appears in Fig. 2(b) as green/turquoise phases. The presence of substantial M_6C in the sintered material is consistent with this material containing an Fe-based binder with a carbon content of about 5.5 wt%, as predicted by Figure 1, which showed the quasi-two-phase region occurs at a carbon content of 5.6-5.7 wt% [13].

3.2 Formation of substrate/coating interface

Having determined the structure of the substrate we now show the coating. Figure 3 shows cross sections of the coating formed after 1, 2 and 4 hours of silicon impregnation at 1000°C. The coatings show a self-similar structure at all times. Thus, as described in a previous report [11], where we reported the coating structure after 4 hours, the coatings at 1 and 2 hours are also clearly composed chiefly of two parts: an upper iron silicide crust, shown as a region of homogenous

contrast, and between that and the substrate, a lower region that is a composite of tungsten disilicide (light contrast) and iron silicides (dark contrast). Beneath that is a porous region. It was determined previously that this two-part structure is crucial to its good oxidation resistance as FeSi oxidises passively, whereas WSi_2 oxidises temperatures below 1300°C in an active manner [16]. However, what was not reported previously was the coating growth kinetics, which we now address in detail as these will allow predictions about how the coating structure may change under different impregnation conditions and cWC compositions.

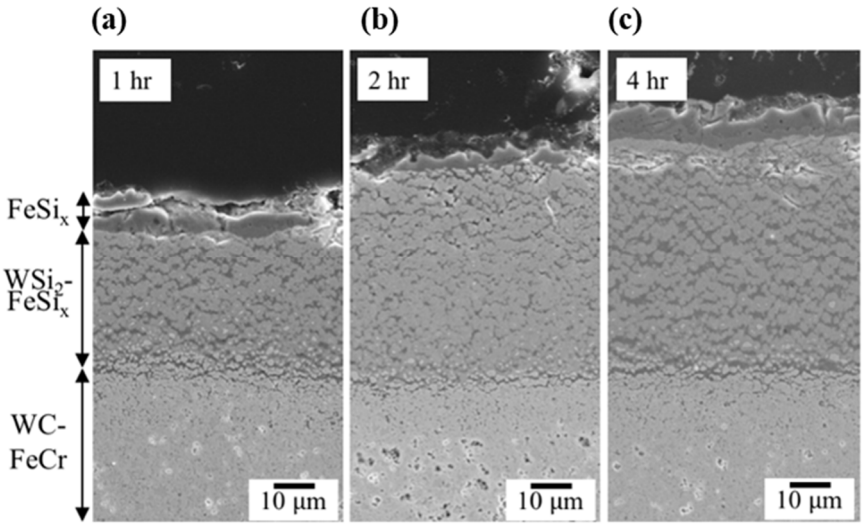

Figure 3: Cross sections of the coating after (**a**) 1, (**b**) 2 and (**c**) 4 hours growth. The phase compositions of the coatings are indicated to the left.

Figure 4 shows the kinetics of coating formation. Part (a) shows the coating growth as measured by both mass change (primary y-axis) and thickness increase (secondary y-axis). Both signals show a parabolic growth kinetics that can be well fitted with a growth constant of 31 µm/hr$^{1/2}$ or 7.5 mg/cm^2-hr$^{1/2}$. This growth rate is then re-plotted in part (b), which is an Arrhenius plot of the growth rates of various other WSi_2 and $FeSi_2$ coatings taken from the literature [16-20]. The WSi_2 growth rates are much slower than $FeSi_2$ for a given temperature. For example, when the WSi_2 growth rates are extrapolated back to 1000°C, the growth constant is predicted to be 10^{-28} - 10^{-31} cm^2/s, whereas the $FeSi_2$ kinetics constants from the literature is on the order of 10^{-20} – i.e. close to what is observed experimentally in this study. The fact that the experimental growth rates match typical growth rates of $FeSi_2$ rather than WSi_2 suggests that mass transport in the binder phase is the dominant mechanism during the formation of these coatings.

Preprints (www.preprints.org) | NOT PEER-REVIEWED | Posted: 1 May 2018 doi:10.20944/preprints201805.0005.v1

Peer-reviewed version available at Coatings 2018, 8, 247; doi:10.3390/coatings8070247

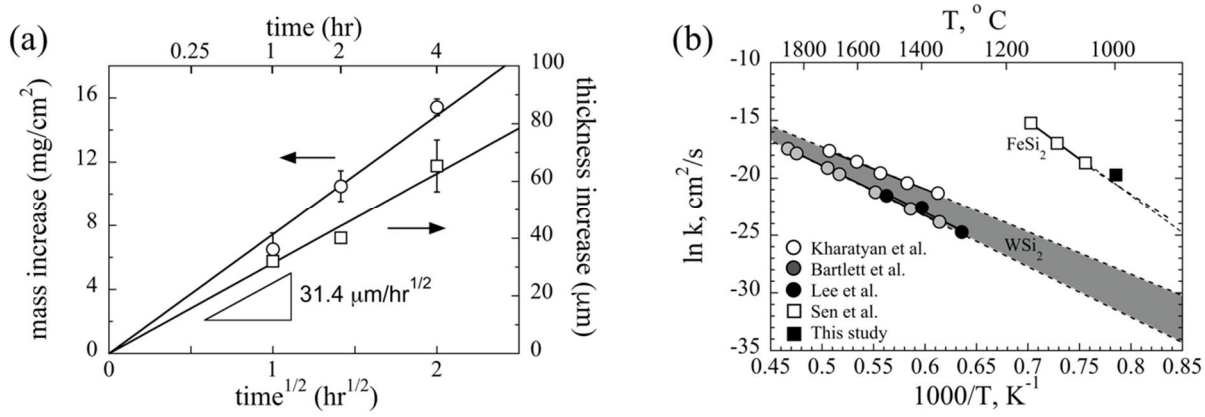

Figure 4: kinetics of coating formation. (**a**) parabolic growth kinetics. Error bars show standard deviation between 3 nominally identical samples. (**b**) Ahrrenius plot comparing to growth kinetics to literature growth rates of WSi_2 (circles) and $FeSi_2$ (squares) [16-20].

This quantitative understanding of the different growth rates of WSi_2 and $FeSi_2$ allows the coating structure shown in Figure 3 to be better interpreted. Specifically, it is of interest to determine whether the two-part structure will always prevail or whether it is possible that WSi_2 could exceed the rate of $FeSi_2$ formation. To assess this, we compare the competition between the formation rates of WSi_2 particles and the $FeSi_2$ binder. The growth rates of these two phases, $k(WSi_2)$ and $k(FeSi_2)$ can be assessed by the literature growth rates shown in Figure 4. To do this we fit Arrhenius equations to the data of Karatayan (WSi_2) [19] and Sen ($FeSi_2$), [20] respectively:

$$k(WSi_2) = 1.36 \exp\left(\frac{35{,}400}{T}\right) \quad (1)$$

$$k(FeSi_2) = 1.58 \times 10^{13} \exp\left(\frac{64{,}900}{T}\right) \quad (2)$$

where T is the growth temperature. To assess the competition between these two phases in a composite, transport in the $FeSi_2$ binder must be modified using the so-called labyrinth factor, λ. This factor represents difference between the bulk diffusivity of the binder phase, and the effective diffusivity of the binder phase when dispersed with a volume fraction, f. The labyrinth factor of $\lambda = f^2$ was reported by Schwarzkopf [21], however this relationship was later rebutted by Frykholm et al [22], who reported it to be $\lambda = f$. Figure 5 therefore considers both possible scenarios. It shows a map – as a function of temperature and volume fraction – of the region in which the transport in the $FeSi_2$ dominates, i.e. the case reported here (labelled "separated coating") and the region where transport in the WSi_2 dominates (labelled "mixed coating"). Two lines delineating these regions are drawn. The two lines correspond to two different labyrinth factors of $\lambda = f^2$ and $\lambda = f$. A "molten region" is also drawn at the binder melting point, at which point the growth rates predicted from Equation 2 would no longer hold. The experimental data of this study, corresponding to $T = 1000$°C and a binder volume factor of $f = 0.18$, is represented by a circle that is located well within the separated coating region, as in agreement with the two-part coating structures shown in Figure 3. The map predicts that such a separated coating will result under most conditions. For example, at $T = 1000$°C, the separated coating is predicted even at a binder content as low as $f = 0.02$ and $f = 0.001$, using labyrinth factors of $\lambda = f^2$ and $\lambda = f$, respectively, which is well below the typical range for cWCs (typically $f = 0.04$ to $f = 0.4$). Furthermore, at the binder volume fraction studied, $f = 0.18$, the separated coating is predicted at temperatures ranging from the binder melting point to ~770-840°C, which is much lower than typical silicon deposition temperatures. Therefore, the structure shown in Figure 3 is predicted to be stable under most experimental scenarios.

Preprints (www.preprints.org) | NOT PEER-REVIEWED | Posted: 1 May 2018 doi:10.20944/preprints201805.0005.v1

Peer-reviewed version available at Coatings 2018, 8, 247; doi:10.3390/coatings8070247

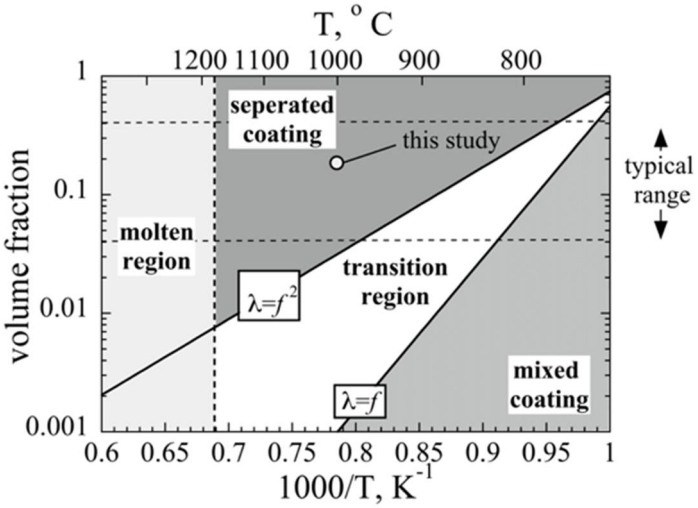

Figure 5: Coating structure growth map as a function of temperature, *T*, and binder volume fraction, *f*. Separated, i.e. two-part, structures are predicted at high *T* and high *f*, and mixed coatings at low *T* and low *f*.

3.3 Coating structure

We now assess the coating phase composition in more detail. Figure 6(a) shows a series of XRD patterns taken through the depth of the coating after 1 hour of silicon deposition. The patterns show a gradual transition in phase composition from the coating surface (i.e. at 0-10 μm), to the coating bulk (10-40 μm) to the substrate (40+ μm). The coating surface is shown to be composed of primarily of two $FeSi_2$ phases – a low temperature orthorhombic $FeSi_2$ phase and a high temperature tetragonal phase which is sub-stoichiometric in iron ($Fe_{0.92}Si_2$). Below this, the coating bulk is primarily a composite of WSi_2 and FeSi, while the substrate is primarily WC and M_6C phase. Figure 6(b) shows the volume fractions of the prominent coating phases, plotted as a function of depth into the coating. The volume fractions are calculated from Rietveld refinements of the diffraction data in part (a). In the volume fraction results, the BCC FeCr phase, α-Fe, has been excluded as its volume fraction was too low to be reliably measured. Furthermore, the two $FeSi_2$ phases have been combined into a single reading, as their peaks overlapped strongly and could therefore not be reliably differentiated. Since this is the first time that the phase composition of these coatings has been mapped spatially, we comment: Firstly, dominance of FeSi and $FeSi_2$ at the surface shows explicitly how the migration of Fe towards the surface occurs. A related point is the lack of significant FeCr binder, within the substrate adjacent to the coating, presumably as it has migrated to the surface. This matches the observations of porosity in substrate in Figure 3. The porous region is shown later to have a significant effect on the mechanical properties of the substrate compared to the specimen bulk. Secondly, the quantification of the phase composition allows the mechanical properties to be properly interpreted, as shown in the following section.

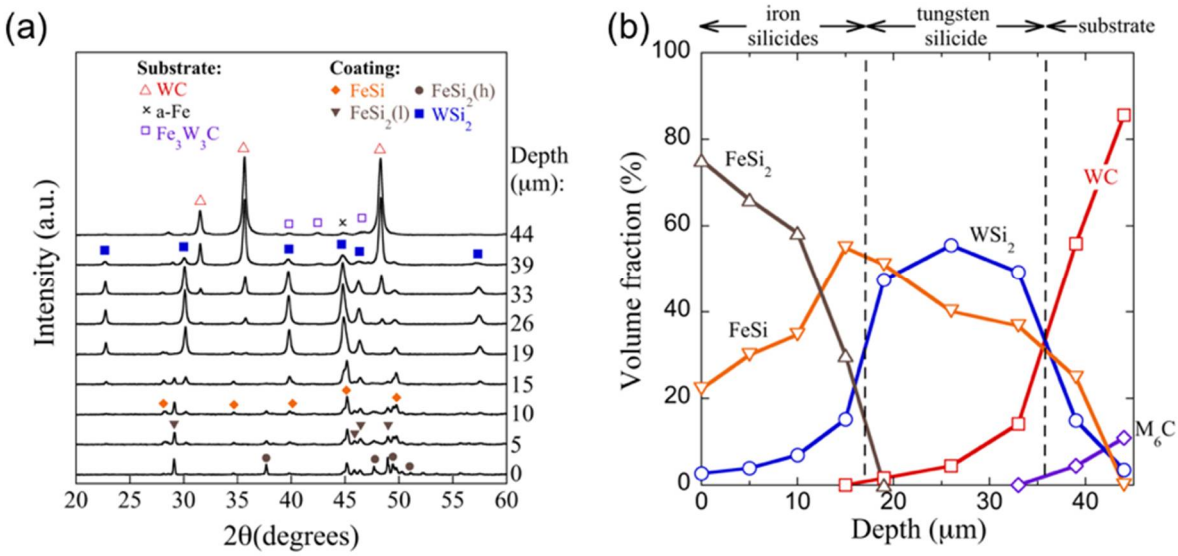

Figure 6: (a) XRD patterns through the thickness of the coating after 1 hour silicon deposition. The surface (0 μm) is predominantly $FeSi_2$ + FeSi. No obvious carbon-containing reaction product between WC and Si is visible. (**b**) Rietveld-determined volume fraction of phases plotted as a function of depth.

Figure 7(a-d) shows some SEM images of the coating at various magnifications. Part (a) shows a large area covering both the substrate and coating: the substrate is shown in the upper section, the coating below it, and the substrate/coating interface in the centre. These areas are magnified in parts (b-d): Part (b), in the substrate region, shows the formation of FeSi regions within the binder. Part (c) shows a WC particle at the interface that has been partially reacted with Silicon to form a core of WC, and a shell of WSi_2. This core-shell structure is magnified in the inset. The WSi_2 shell contains very fine laths of a dark contrast, growing normal to the advancing WC/WSi_2 interface. These laths can also be seen in a region of the coating that has fully reacted in parts (d). Their very fine thickness of <100 nm, and growth direction, i.e. perpendicular to the WC/WSi_2 interface, suggests they form as a by-product of the silicidation reaction. Their dark contrast indicates they are also predominantly low-Z. To elucidate their composition, part (e) shows an XRD pattern taken from within the bulk of the coating (at a depth of 26 μm in Figure 5). The pattern is plotted on a logarithmic scale to elucidate minor peaks. Below the pattern, simulated patterns of phases identified in Figure 6 are shown – i.e. WSi_2, WC and FeSi. However, one very low intensity peak remains unidentified at 60 degrees, which is well matched to the cubic SiC phase. This suggests that the dark laths are cubic SiC, which are assumed to form via the reaction:

$$WC + 3Si \rightarrow WSi_2 + SiC \quad (3)$$

Although their volume fraction could not be determined from the XRD data, if reaction (3) proceeds to completion, on the basis of the relative densities of the product phases, the volume fraction of SiC within the WSi_2 phase would be approximately 0.326. With this microstructural understanding we now assess mechanical properties.

Preprints (www.preprints.org) | NOT PEER-REVIEWED | Posted: 1 May 2018 doi:10.20944/preprints201805.0005.v1

Peer-reviewed version available at Coatings 2018, 8, 247; doi:10.3390/coatings8070247

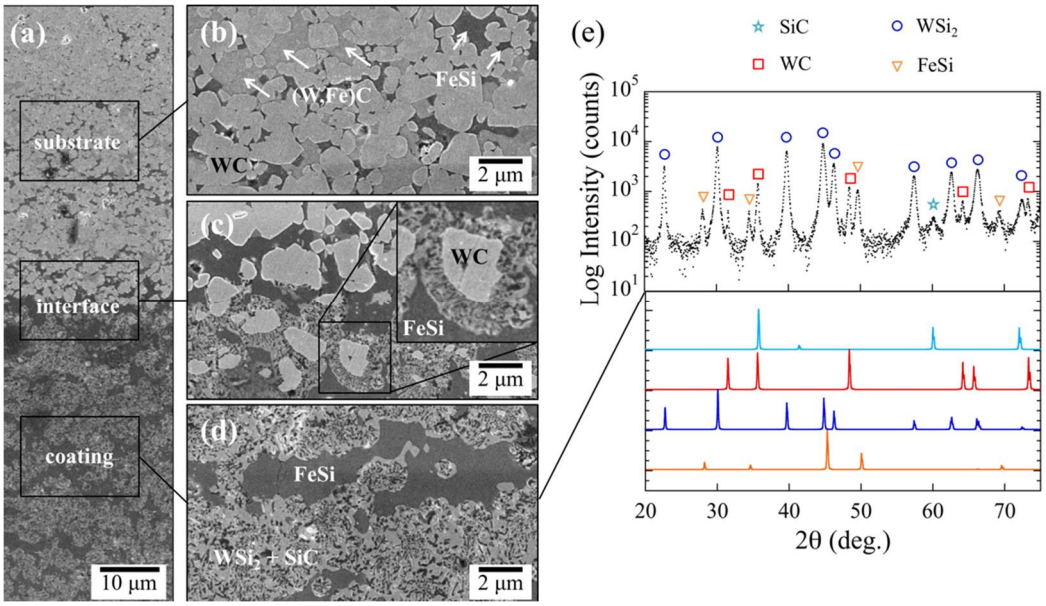

Figure 7: (**a**) overview SEM image and (**d-b**) magnified SEM images of coating. Inset of part (**c**) a WC particle in the process of reacting with FeSi to form a WSi_2 (light contrast) and SiC (dark). Corresponding XRD spectra from (**d**) is shown in (**e**).

8.4 *Coating mechanical properties*

Figure 8 shows the instrumented microhardness tests of the coating. Part (a) shows an SEM image of a 6x16 array of indents. I.e. 16 vertical columns, where within each, i.e. for a given depth location within the coating, 6 nominally identical indents are made. Each indent is spaced 15 μm apart. The magnified areas in part (a) show typical indents in each region of the coating, i.e. the substrate (red), the porous region immediately below the substrate (green), and in the bulk of the coating (blue). Part (b) shows a typical load-displacement curves taken from each region. For a given load, the overall depth of displacement for the coating was lower than in the substrate bulk, while it was higher for the porous zone, indicating the coating is harder – and the porous zone softer – than the bulk.

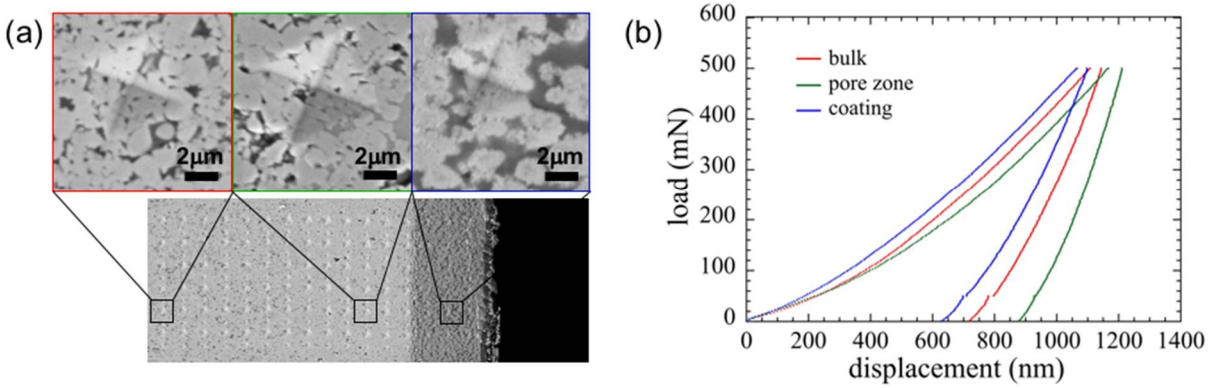

Figure 8: (**a**) overview of the indentation array, with magnified images of the bulk (left), pore zone (middle) and coating (right). Part (**b**) typical load-displacement curves for each zone.

A more quantitative picture of the hardness evolution is shown in Figure 9. Part (a) shows the hardness profile into the coating. Each reported hardness value represents the mean of 6 nominally

identical indents, although in a limited number of cases where an indent had to be rejected, 5 indents were used. The hardness shows near-constant values in each region of the coating. The substrate bulk hardness is 23.6 ∓ 0.5 GPa; the pore zone of the substrate is 20.3 ∓ 0.4 GPa; and the coating hardness is 28.3 ∓ 1 GPa. The corresponding modulus values are plotted in part (b). Here, the modulus in the substrate and the pore zone are the same, which can be explained by densification of pores under the indenter tip, and thus similar unload behaviour. The average modulus is 550 ∓ 20 GPa. This is close to what is expected based on the modulus of the constituent phases. For example, using a rule of mixtures, employing the modulus of WC and ferritic steels, (given as 705 GPa and 200 GPa [23], respectively), in relative volume fractions of 0.82 and 0.18 respectively, yields a predicted modulus of 614 GPa. Our measured Young's modulus on the substrate is therefore within 10% of the prediction, indicating the data is physically meaningful.

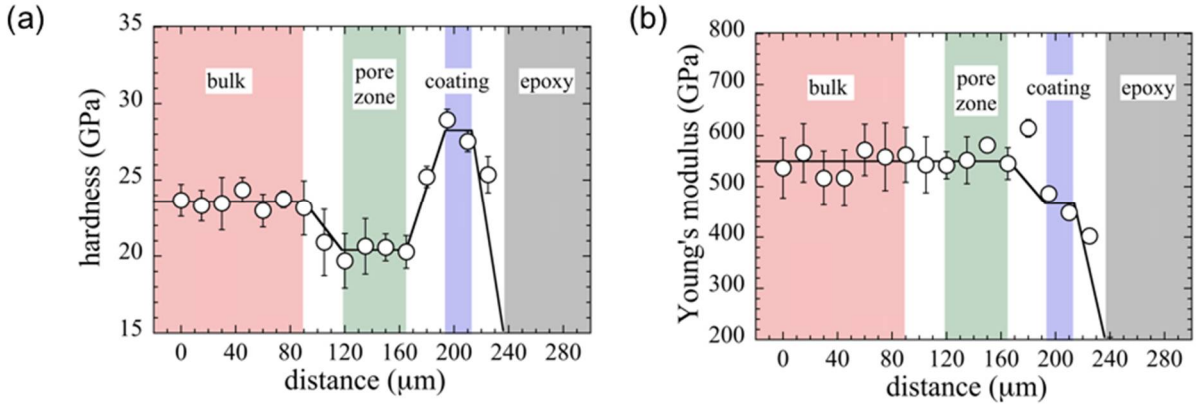

Figure 9: Evolution in hardness (**a**) and Young's modulus (**b**) into the coating depth. Error bars represent the standard deviation of at least 5 nominally identical indents.

The substrate nanohardness values in Figure 9 are higher than those macrohardness values reported in Table 1. We now consider these difference in detail: The hardness of the substrate at 500mN of load, 23.6 GPa, is about 60 % higher than the macrohardness value at 30 kgf (294 N), which was 14.6 GPa (see Table 1). This indentation size effect is commonly observed in cWCs when indented at different length scales [24]. For example, Roebuck et al [25] reported an order of magnitude increase in the hardness of WC-11 wt.% Co when tested at 1mN vs its macrohardness value. In a less extreme range of indenter sizes, Nabarro et al [22] indented a WC-11 wt.% Co sample over a load range of about 50mN-10N, and observed about a 50% hardness rise, i.e. a similar increase to the present study, for a similar load change (200-fold vs 600-fold for our study). Thus, the indenter size effect in WC-FeCr materials appears to be roughly in keeping with similar materials indented across a comparable range of loads.

Despite the absolute magnitude of hardness values reported in Figure 9 being size-dependent, insight can be gained by assessing the relative magnitudes. We now consider the hardness of the coated layer, whose average value of 28.3 GPa is 20% higher than the substrate. To rationalise this observation, Table 2 shows the constituent phases of the coating, along with their corresponding literature hardness values and observed volume fractions, V_f. The volume fractions labelled are calculated by taking the X-ray determined volume fractions from the centre of the coating, i.e. at 26 μm in Figure 5 and re-calculating on the basis of Equation (1), which predicts that SiC forms in equimolar proportions and thus at about half the volume of WSi_2 (0.326 vs. 0.674). The hardness values are Vickers measurements (at loads of 25-300N) from the literature [23, 26].

Table 2: volume fractions of coating phases and corresponding literature hardness values.

Phase	WC	FeSi	WSi_2	SiC
V_f	0.04	0.3	0.43	0.22
Hardness (GPa)	23.5	9.3	10.7	31.9

Using the rule-of-mixtures, the peak hardness of the coating is estimated to be 15.3 GPa. Thus, the experimentally measured value of 28.3 GPa is about 80% higher than this. This is quite close to the 60% higher hardness value measured in the substrate, which is attributed to indenter size effect. However, we note that the above analysis is very coarse in nature for the following reasons: Firstly, the analysis assumes the coating is homogenous, whereas Figure 5 shows it is not, and therefore our results are subject to uncertainty from sampling statistics; secondly, it neglects any size effects in the single-phase hardness values taken from the literature; and thirdly, it assumes ideal composite behaviour, when in fact, there may be multiple hardening mechanisms in operation.

Finally, we address the hardness of the porous zone, immediately beneath the coating. Being about 14% lower than the bulk, this may have a detrimental effect on the coating stability. However, it is possible that this could be remedied by two methods: the first is a heat treatment above the binder melting point of 1180 ° C, after the coating application, where we envisage that excess binder from the substrate could migrate to re-fill the pores. We note, however, that the binder melting temperature is also close to the melting temperature of the $FeSi_2$(h) phase, of 1209 ° C. It is therefore unknown what effect such heat treatments would have on the structure and efficacy of the coating. The second method we suggest is to process the composite to have a higher binder content in the starting substrate in the near surface region. One way of achieving this would be to modify the sintering conditions such that a layer of binder phase migrates to the surface during cooling from liquid phase [28]. This technique is well known for a wide variety of cermets [28] and is typically used when brazing or coating treatments are required post annealing. Such investigations therefore present an opportunity for further work.

4. Conclusions

Following a recent demonstration of the oxidation resistance of silicide-coated cWCs [11], this work has investigated the growth kinetics, phase structure, and mechanical properties of such coatings. The main conclusions are as follows:

- The coating formation kinetics show that growth is dominated by the formation of iron silicide. By analysing the growth kinetics as trade-off between transport within the carbide grains and the binder we show that the two-part, passively oxidising (protective) structure, with be dominant under most experimental scenarios. However, at very low silicon deposition temperatures and at very low volume fractions of binder, such a two-part structure may not occur.
- By analysing the structure using quantitative diffraction measurements and high-resolution electron microscopy, the formation of nano-scale SiC laths was observed within the WSi_2 domains, which was not previously understood in our original report [11].
- The most surprising aspect of this study was the very high hardness of the coating, which was about 20 % higher than that of the substrate. The impressive mechanical properties of the coating show promise for their engineering applications and could be explained based on the composite nature of the WSi_2/SiC particles and their respective literature hardness values.
- The porous region immediately below the substrate had a hardness 14 % lower than the bulk, which was explained via a net transport of FeCr binder towards the coating/substrate interface. This porous region is potentially detrimental to the coating's properties but could

be mitigated by enhancing the near-surface binder content or using liquid phase heat-treatments after coating deposition.

References

1. Clery, D. The new shape of fusion. *Science* **2015**. 348 pp 854-856
2. http://www.allaboutcementedcarbide.com Retrieved on 15.09.2017 (c)Sandvik AB.
3. Matthews, G.F., et al., The second phase of JET operation with the ITER-like wall. *Physica Scripta* **2014**. T159.
4. Windsor, C.G. and J.G. Morgan, Neutron and gamma flux distributions and their implications for radiation damage in the shielded superconducting core of a fusion power plant. *Nucl. Fusion* **2017**. 57: pp. 116032.
5. Windsor, C.G., et al., Modelling the power deposition into a spherical tokamak fusion power plant. *Nucl. Fusion* **2017**. 57(3): pp. 036001.
6. Alexander, P., *Atomic Radiation and Life*. 2nd ed. **1957**. Chapter 5.
7. Webb, W.W., J.T. Norton, and C. Wagner, Oxidization studies in metal-carbon systems. *J. Electrochem. Soc*. **1956**. 103: pp. 112-117.
8. Humphry-Baker, S.A., et al., Thermophysical properties of Co-free WC-FeCr hardmetals. *Int. J. Refract. Met. Hard Mater.* (Plansee 2017 Special Issue), **2018**.
9. Humphry-Baker, S.A. and W.E. Lee, Tungsten carbide is more oxidation resistant than tungsten when processed to full density. *Scripta Mater.*, **2016.** 116: pp. 67-70.
10. D. Maisonnier et al.The European power plant conceptual study, *Fusion Eng. Des.* **2005**. 75–79: pp 1173–1179.
11. Humphry-Baker, S.A., K. Peng, and W.E. Lee, Oxidation resistant tungsten carbide hardmetals. *Int. J. Refract. Met. Hard Mater.* **2017**. 66: pp. 135-145.
12. Oliver, W., and Pharr, G. An improved technique for determining hardness and elastic modulus using load and displacement sensing indentation experiments. *J. Mater. Res.* **1992.** 7(6): pp. 1564-1583.
13. Guillermet, A. F. The Co-Fe-Ni-W-C Phase Diagram: A Thermodynamic Description and Calculated Sections for (Co-Fe-Ni) Bonded Cemented WC Tools. *Zeit. für Metall.* **1989.** 80(2): pp. 83-94.
14. Mingard, K.P., et al. Some aspects of the structure of cobalt and nickel binder phases in hardmetals. *Acta Mater.* **2011**. 59(6): pp. 2277-2290.
15. Marshall, J.M. and A. Kusoffsky, Binder phase structure in fine and coarse WC-Co hard metals with Cr and V carbide additions. *Int. J. Refract. Met. Hard Mater* **2013**. 40: pp. 27-35.
16. Kim, H.S., et al., Growth behavior and microstructure of oxide scales grown on WSi2 coating. *Intermetall.* **2008**. 16(3): pp. 360-372.
17. Lee K-H, Yoon J-K, Lee J-K, et al. Growth kinetics of W_5Si_3 layer in WSi_2/W system. Surf Coat Technol **2004** 187: pp 146–153
18. R.W. Bartlett, P.R. Gage, P.A. Larssen, Diffusion kinetics affecting formation of silicide coatings on molybdenum and tungsten. *Trans. TMS-AIME* **1964** 230: pp 1582
19 S.L. Kharatyan, H.A. Chatilyan, A.B. Harutyunyan, High temperature diffusivities in the Mo_5Si_3 and W_5Si_3 phases. *Defect Diffus. Forum, Sci. Publ.* (**2001**) 1557: pp 194– 199
20. Sen U, Ozdemir O, Yilmaz S, Şen S Kinetics Of Iron Silicide Deposited On AiSi D2 Steel By Pack Method. Proceedings of the 22nd International Conference on Metallurgy and Metals. Brno, Czech Republic 15-17th May 2013
21. Schwarzkopf, M., Kinetik der Bildung von Mischkarbidfreien Randzonen auf Hartmetallen. PhD thesis. Montanuniversität Leoben. Leoben, Austria. **1987**.
22. Frykholm, R., et al., Effect of cubic phase composition on gradient zone formation in cemented carbides. *Int. J. Refract. Met. Hard Mater.* **2001**. 19(4-6): pp. 527-538.

23. Shackelford JF, Han Y-H, Kim S, Kwon S-H. **2016.** *CRC Materials Science and Engineering Handbook*. CRC press
24. A.V. Shatov, S.S. Ponomarev, S.A. Firstov Hardness and deformation of hardmetals at room temperature. *Comprehensive Hard Materials*,V.K. Sarin, D. Mari, L. Llanes (Eds.), **2014.** 1 Elsevier , pp. 647-699
25. Roebuck, B., Terminology, testing, properties, imaging and models for fine grained hardmetals. *Int. J. Refract. Met. Hard Mater.* **1995**. 13(5): pp. 265-279.
26. Milekhine V, Onsøien MI, Solberg JK, Skaland T S. Mechanical properties of FeSi (ε), FeSi2 (ζα) and Mg2Si. *Intermetallics* **2002.** 10 :pp 743–750
27. Nabarro, F.R.N., S. Shrivastava, and S.B. Luyckx. The size effect in microindentation. *Philo. Mag.,* **2006**. 86(25-26): pp. 4173-4180
28. José Garćia, Sven Englund and Fredrik Haglöf. Controlling Co cappling in sintering process of cermets. *Int. J. Refract. Met. Hard Mater.* **2017.** 62: pp26-133

Acknowledgements

SHB thanks the Imperial College Research Fellowship for financial support. The authors would also like to thank Sandvik Hyperion for providing the hardmetal sample used in this study.